Acta Materialia 224 (2022) 117532

Contents lists available at ScienceDirect

Acta Materialia

journal homepage: www.elsevier.com/locate/actamat

Full length article

Magnetocaloric effect in the $(Mn,Fe)_2(P,Si)$ system: From bulk to nano

Fengqi Zhang[a,*], Chris Taake[b], Bowei Huang[a], Xinmin You[a], Hamutu Ojiyed[a], Qi Shen[a], Iulian Dugulan[a], Luana Caron[b,c], Niels van Dijk[a], Ekkes Brück[a]

[a] Fundamental Aspects of Materials and Energy (FAME), Faculty of Applied Sciences, Delft University of Technology, Delft, the Netherlands
[b] Department of Physics, Bielefeld University, Bielefeld, Germany
[c] Helmholtz-Zentrum Berlin für Materialien und Energie, 12489 Berlin, Germany

ARTICLE INFO

Article history:
Received 24 September 2021
Revised 26 November 2021
Accepted 27 November 2021
Available online 30 November 2021

Keywords:
Magnetocaloric materials
(Mn,Fe)2(P,Si)
Nanoparticles
Magnetization
Phase transition

ABSTRACT

In the field of nanoscale magnetocaloric materials, novel concepts like micro-refrigerators, thermal switches, microfluidic pumps, energy harvesting devices and biomedical applications have been proposed. However, reports on nanoscale $(Mn,Fe)_2(P,Si)$-based materials, which are one of the most promising bulk materials for solid-state magnetic refrigeration, are rare. In this study we have synthesized $(Mn,Fe)_2(P,Si)$-based nanoparticles, and systematically investigated the influence of crystallite size and microstructure on the giant magnetocaloric effect. The results show that the decreased saturation magnetization (M_s) is mainly attributed to the increased concentration of an atomically disordered shell, and with a decreased particle size, both the thermal hysteresis and T_c are reduced. In addition, we determined an optimal temperature window for annealing after synthesis of 300–600 °C and found that gaseous nitriding can enhance M_s from 120 to 148 Am^2kg^{-1} and the magnetic entropy change (ΔS_m) from 0.8 to 1.2 $Jkg^{-1}K^{-1}$ in a field change of $\Delta\mu_0H = 1$ T. This improvement can be attributed to the synergetic effect of annealing and nitration, which effectively removes part of the defects inside the particles. The produced superparamagnetic particles have been probed by high-resolution transmission electron microscopy, Mössbauer spectra and magnetic measurements. Our results provide important insight into the performance of giant magnetocaloric materials at the nanoscale.

1. Introduction

The magnetocaloric effect (MCE) describes the fundamental phenomenon that when a magnetic compound is exposed to a change in the applied magnetic field under adiabatic conditions it shows an increase or decrease in temperature. This adiabatic temperature change ΔT_{ad} is associated with a transfer between magnetic and vibrational entropies. In magnetocaloric materials (MCMs) the strength of the MCE is affected by several intrinsic factors like the chemical composition, the crystal structure, the nature of the magnetic interactions and the stress state. Since the seminal work on the discovery of GdSiGe-based MCMs by Pecharsky and coworkers in 1997 [1], a growing number of first-order magnetic transition (FOMT) materials, which demonstrate a giant magnetocaloric effect (GMCE) have sprung up. This contrasts with most other magnetic materials that show a second order magnetic transition (SOMT). Currently, numerous promising GMCE candidate materials have been proposed, including $(Mn,Fe)_2(P,X)$-based compounds (X = As, Ge, Si) [2–4], $La(Fe,Si)_{13}$-based materials [5], NiMn-X based Heusler alloys (X = Ga, In, Sn, Sb) [6], FeRh based alloys [7], Mn_2Sb based alloys [8] and MnM-X (M= Co or Ni, X= Si or Ge) ferromagnets [9]. These MCMs with a GMCE exhibit the potential to design efficient devices for solid state magnetic refrigeration, magnetic heat pumps and energy harvesting.

Among these MCMs, the $(Mn,Fe)_2(P,Si)$-based alloys, together with the $La(Fe,Si)_{13}$-based alloys, are the most promising giant MCMs [10] and have been widely investigated because of their excellent GMCE performance, low economic costs and absence of toxic elements, in comparison with previous two-generation $(Mn,Fe)_2(P,As)$ and $(Mn,Fe)_2(P,Ge)$-based compounds. Interestingly, the magneto-elastic coupling in $(Mn,Fe)_2(P,Si)$-based MCMs (accompanied by a change in c/a ratio at the FOMT) enables a reduction in thermal hysteresis (ΔT_{hys}) by doping [11]. In addition, the Curie temperature (T_C) can be tuned by composition within a wide temperature window (100–500 K) [12]. In MCMs like the NiMn-based Heusler alloys the magneto-structural coupling leads to a drastic change in crystal structure resulting in a relatively large value for ΔT_{hys}, which is detrimental for the cycling efficiency. The physical mechanism responsible for the GMCE in the $(Mn,Fe)_2(P,Si)$-based MCMs originates from the so-called "mixed

* Corresponding author.

https://doi.org/10.1016/j.actamat.2021.117532

magnetism". The interlayers of the crystallographic 3 g (preferentially occupied by Mn) and the crystallographic 3*f* sites (preferentially occupied by Fe) of the hexagonal lattice, represent layers with relatively large stable magnetic moments and relatively weak unstable magnetic moments, respectively. The latter show an interesting "moment-quenching" property across the magnetic transition, as indicated by density functional theory (DFT) [13], neutron diffraction (ND) [14] and X-ray magnetic circular dichroism (XMCD) [15]. Combined DFT calculations and synchrotron high-resolution X-ray diffraction (HRXRD) [16] experiments show a significant electronic charge redistribution around the Fe atoms across the ferromagnetic transition, which was attributed to the competition between magnetism and covalent bonding.

However, although extensive experimental and theoretical studies have focused on the characterization of bulk $(Mn,Fe)_2(P,Si)$-based GMCE materials, the relationship between the magneto-elastic coupling and a size reduction down to nanoscale particles is still pivotal and deserves further exploration. In the field of nanoscale GMCE materials, some novel devices have been proposed in the field of micro-refrigerators [17,18], thermal switches [19], microfluidic pumps [20,21], energy harvesting devices [22,23] and biomedical applications (magnetic hyperthermia [24] or drug delivery [25]). Nano-sized particles have several properties that are distinctly different from bulk materials, like a high surface-to-volume ratio and a fast thermal response. Nonetheless, reports about nanoscale $(Mn,Fe)_2(P,Si)$-based GMCE materials are rare. In this paper, nanoscale $(Mn,Fe)_2(P,Si)$-based MCMs were produced by a "top-down" wet high-energy mechanical milling (HEMM) method [26], which is cheap and can be easily scaled up. The refined particle size distribution in this method is a result of repetitive fragmentation and coalescence events. The crystal structure, thermodynamics and magnetization are investigated as a function of crystallite size. A moderate post-milled annealing at a temperature of 300–600 °C under N_2 atmosphere was found to efficiently recover the bulk MCE as a result of the synergistic effect of gaseous nitridation and the removal of dislocations in the particles, as observed by High-resolution transmission electron microscopy (HRTEM). Combined HRTEM, temperature-dependent Mössbauer spectroscopy and magnetic measurements, reveal the presence of a mono-domain state in $(Mn,Fe)_2(P,Si)$-based superparamagnetic particles. Our findings shed new light on the properties of nanoscale GMCE materials and offer useful guidelines for practical engineering applications like ferro-fluids for self-pumping applications.

2. Experimental procedure

Bulk $MnFeP_{0.45}Si_{0.55}$ MCMs were synthesized from 10 g mixed powders of Mn (99.9%), Fe (99.9%), red-P (99.7%) and Si (99.9%) by milling for 10 h at 380 rpm. To prevent iron contamination, tungsten carbide (WC) balls were used during the pre-alloying procedure. The resulting powders were then pressed into cylindrical tablets sealed in quartz tubes under Ar atmosphere and then annealed for 25 h at 1373 K. After that, these samples were rapidly quenched in cold water, followed by a pre-cooling process in liquid nitrogen to remove the so-called "virgin effect" [27]. Subsequently, 5 g bulk samples and 3 ml oleic acid (chemical surfactant to passivate surface and prevent oxidation), were mixed together with 2-propanol under Ar atmosphere. The synthesis scheme is illustrated in Fig. S1 (Supplementary Information). During the whole procedure, we keep the same ball/powder weight ratio (8:1). Correspondingly, 0.3 g ball-milled powder was taken out from the jar at different ball milling (BM) times ranging from 1 to 26 h (ball milling times of 1, 2, 4, 8, 12, 16, 20, 26 h were used). The residual surfactant and 2-propanol on the surface of milled-powders can be removed completely by mixing with an anhydrous ethanol solution and high-speed centrifugation (10,000 rpm). To recover the magnetic properties after ball milling, we processed the milled powders (e.g. 26 h) in a horizontal tubular furnace under N_2 flow in different annealing temperatures (300, 500, 550, 600, 700 and 900 °C). For comparison, Ar atmosphere is also applied at an annealing temperature of 600 °C. The average powder size of the BM-0 h raw material is around 100 μm. The SEM and corresponding EDS mapping images can be found in Fig. S2 (Supplementary Information).

Differential scanning calorimetry (DSC) measurements were carried out using a TA-Q2000 DSC calorimeter. In the high temperature paramagnetic (PM), state X-ray diffraction (XRD) patterns were collected using an Anton Paar TTK450 temperature-tunable sample chamber and a PANalytical X-pert Pro-diffractometer with Cu K_α radiation. The crystal structure refinement of the XRD patterns was performed using Fullprof's implementation of the Rietveld refinement method [28]. The average crystallite size was calculated based on the Scherrer equation implemented in the X'pert Highscore software. Field-dependent magnetization (*M-H*) curves at a temperature of 5 K were measured in a magnetometer equipped with a superconducting quantum interference device (SQUID, Quantum Design MPMS 5XL) and a vibrating-sample magnetometer (VSM, Quantum Design Versalab) was used to measure temperature-dependent magnetization (*M-T*) curves. Transmission ^{57}Fe Mössbauer spectroscopy experiments at 4.2 and 130 K were performed on a spectrometer using a $^{57}Co(Rh)$ source with a sinusoidal velocity transducer. The velocity calibration was carried out using an α-Fe foil at room temperature. The source and the absorbing samples were kept at the same temperature during measurements. The Mössbauer spectra were fitted using the Mösswinn 4.0 program. The spectra were fitted with a binomial distribution model, as previously described for the analysis of Mössbauer spectra of $FeMnP_{1-x}As_x$ compounds [29]. To prove the surface functionalization of surfactant, diffuse reflectance infrared Fourier transform (DRIFT) spectroscopy measurements were performed on a Thermo Nicolet Nexus 670 with a Harrick reflectance device with KBr as reference material, over the range 4000 to 400 cm^{-1}. DRIFT experiments show the used surfactant can be easily removed after a high-speed centrifugation process, as shown in Fig. S12 (Supplementary Information). All demonstrated samples went through this process. Scanning electron microscopy (SEM) was carried out on a JSM-7500F Field Emission Scanning Electron Microscope to study the particle distribution. HRTEM analysis was performed using a Jeol JEM 2200FS (200 keV) and the element distributions were measured with the EDX detector of the same microscope in mapping mode. Digital image processing was performed by the DigitalMicrograph software (version 3.9.1, Gatan Inc).

3. Results and discussion

3.1. Crystal structural information and average crystallite size

The XRD patterns of original bulk $MnFeP_{0.45}Si_{0.55}$ material in the high-temperature PM state are shown in Fig. 1a. The hexagonal Fe_2P-type (space group *P*-62*m*) phase was identified as the main phase. In addition, a cubic $(Mn,Fe)_3Si$-type impurity phase (space group *Fm*-3*m*) was observed with a weight fraction of 10.1(2) wt.%. In the inset of Fig. 1a, the hexagonal $(Mn,Fe)_2(P,Si)$ crystal structure has been illustrated, where the Mn atoms (red) preferentially occupy the pyramidal coordinated 3*g* sites with five nonmetal nearest neighbors, while the Fe atoms (blue) favor the tetragonal coordinated *3f* sites surrounded by four nonmetal coordination atoms and the P (Si) atoms are randomly distributed on the *2c* and *1b* sites [30].

To investigate the influence of the high-energy ball milling (HEBM) process on the crystal structure, the XRD patterns of $MnFeP_{0.45}Si_{0.55}$ powders were obtained for different BM times in

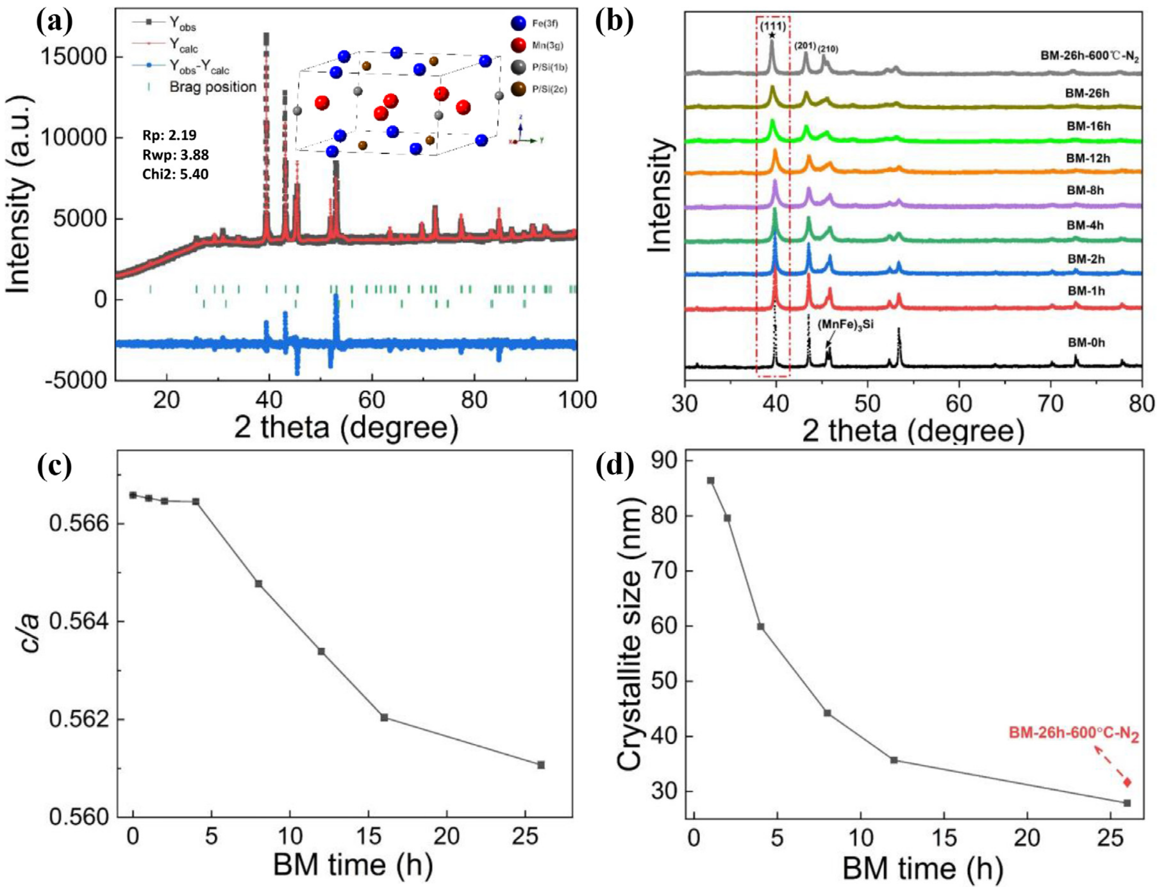

Fig. 1. (a) High-temperature XRD patterns of bulk $MnFeP_{0.45}Si_{0.55}$ material in the PM state. (b) XRD patterns of $MnFeP_{0.45}Si_{0.55}$ samples as a function of the BM times (0, 1, 2,4, 8, 12, 16, 20 and 26 h) and post-annealed condition (600 °C and N_2 atmosphere) in the PM state. (c) The *c/a* ratio as a function of BM times. (d) Average crystallite size as a function of the BM time obtained from the peak width of the diffraction peaks.

the PM state, as shown in Fig. 1b. The three strongest reflections (111), (201) and (210) of the hexagonal structure in the milled powders indicate that the overall structure is largely unchanged. In Fig. 1c the hexagonal lattice parameters ratio *c/a* are presented (*a, c* and the volume *V* can be found in Fig. S3 (Supplementary Information)). It can be seen that *c/a* only slightly changes for BM times up to 4 h and it decreases dramatically for longer BM times. As seen in Fig. 1b, the XRD peak-heights decrease, while the peaks broaden for increasing BM times. The peak broadening results from a decreased particle size and introduced micro-strains during BM process. The average crystallite size of the ball-milled samples is estimated based on Scherrer equation $D_{hkl} = K\lambda/(B_{hkl}\cos(\theta))$, where D_{hkl} is the average crystallite size, *hkl* are Miller indices of the crystal planes, *K* is the crystallite-shape factor (0.9), λ is the wavelength of the X-rays (0.154 nm for Cu $K_{\alpha 1}$ radiation), B_{hkl} is the full-width at half-maximum (FWHM) of the diffraction peak in radians and θ is the Bragg angle [31]. Note, that estimation of the crystallite size from the peak width in the XRD patterns is only reliable up to a crystallite size of about 200 nm. The influence of microstrains on the peak width was not considered during calculation because: (*i*) the crystallite size generally contributes more to the peak broadening than the microstrains when crystallite size is below 100 nm [32] and (*ii*) the strongest low-angle XRD peak ((111) reflection) was chosen to estimate the crystallite size as the contribution of microstrains to peak broadening is relatively small in the low-angle range [33,34].

As shown in Fig. 1d, the average crystallite size gradually reduces from 86 nm (BM-1 h) to 28 nm (BM-26 h), with a slight increase to 32 nm for the sample that was annealed after ball milling (BM-26h-600 °C–N_2). Previous studies showed that the crystallite size increases exponentially with increasing annealing temperature [35]. The slower increase for our samples may result from the moderate annealing temperature and from the nitrogen surface passivation, which is also observed in steels and Li-ion battery materials [36,37]. The average crystallite size for bulk $(Mn,Fe)_2(P,Si)$ based MCMs with coarse grains is around 27 μm [38]. Here it is found that even a BM time of 1 h significantly decreases the crystallite size to nanoscale, which might be caused by the drastic plastic deformation and the continuous fracturing during the HEBM process. In contrast to the significant reduction in crystallite size for BM times up to 4 h, successive ball milling results in a slow decrease in crystallite size towards a limiting value of around 30 nm, this may be governed by the hardening rate introduced by the dislocation generation and the recovery rate arising from dislocation annihilation and recombination [39]. Additionally, the continuous decrease in crystallite size in Fig. 1d is correlated with the decrease in *c/a* ratio in Fig. 1c because the *c/a* ratio is closely related to the magnetic exchange coupling [40]. The microstructure of the BM samples will be investigated in detail in Section 3.4.

3.2. Thermodynamic properties

Fig. 2a shows the DSC curves of different BM samples performed on cooling/heating processes between 360 and 415 K. The sharp exothermic and endothermic peaks for samples with a short BM time (less than 12 h) correspond to the presence of a FOMT, while the samples with a longer BM time (e.g. 26 h) show a less pronounced specific heat peak. This indicates that long BM times

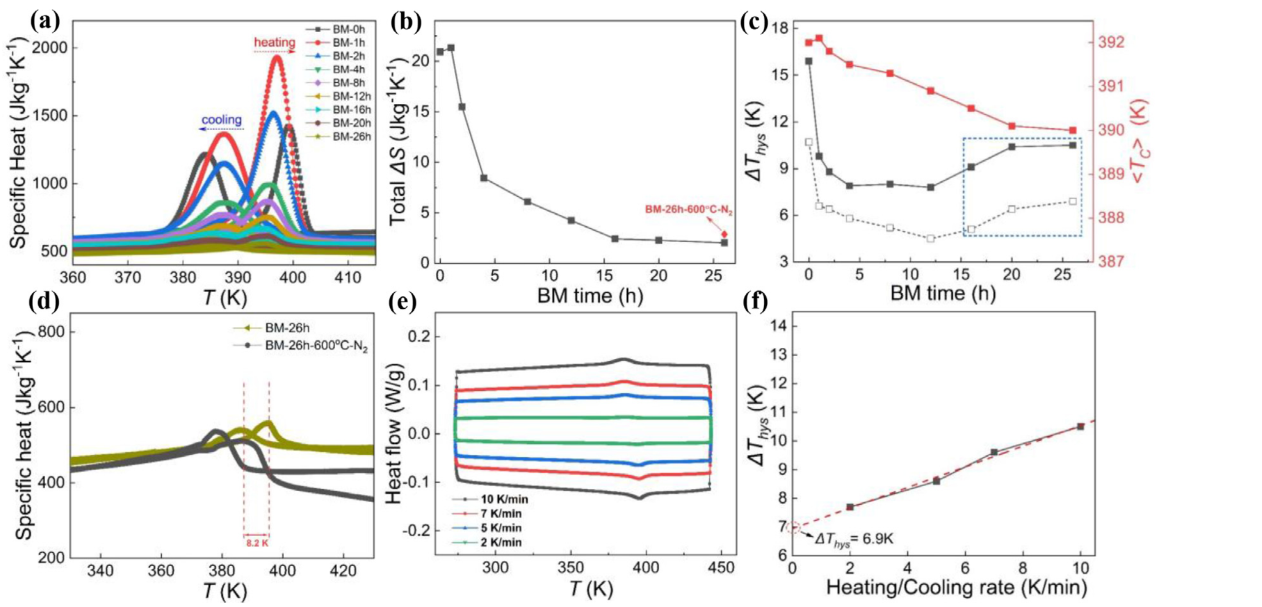

Fig. 2. (a) Zero-field DSC curves of $MnFeP_{0.45}Si_{0.55}$ samples for different BM times along with heating and cooling process. (b) The ΔS_{tot} as a function of BM times; (c) The changes in the thermal hysteresis ΔT_{hys} and the average Curie temperature $\langle T_C \rangle = (T_C{}^{heating} + T_C{}^{cooling})/2$ for different BM times. (d) DSC curves of the BM-26 h and BM-26h-600 °C–N_2 samples. (e) DSC curves at different heating/cooling rates for BM-26 h sample. (f) Linear fitting of ΔT_{hys} obtained from different sweep rates for the BM-26 h sample.

shift the FOMT towards the boundary between the FOMT and the SOMT. The total entropy change (ΔS_{tot}) at T_C is determined by equation $\Delta S_{tot} = L/T_C$, where L is the latent heat, which was derived from the temperature integral of the specific heat (after subtraction of a linear background). As shown in Fig. 2b, compared with the bulk sample ($\Delta S_{tot} = 20.93$ $Jkg^{-1}K^{-1}$), the sample with a BM time of 26 h only shows roughly 10% ($\Delta S_{tot=}2.03$ $Jkg^{-1}K^{-1}$) of the original bulk value, but the post-annealed sample (BM-26h-600 °C–N_2) shows a partial recovery ($\Delta S_{tot} = 2.86$ $Jkg^{-1}K^{-1}$). From Fig. 2c, it is observed that ΔT_{hys} (which is determined by the distance between exothermic and endothermic peaks) sharply decreases from 15.9 to 7.8 K for increasing BM times up to 12 h. For longer BM times it increases slightly, which may be ascribed to the growing amount of defects like dislocations introduced in the material (see HRTEM results in Section 3.3). The $\langle T_C \rangle = (T_C{}^{heating} + T_C{}^{cooling})/2$ exhibits a similar decreasing tendency with increasing BM time.

This reflects that the BM effectively reduces the atomic exchange interaction energy and the exchange integral (J_{ex}) that controls the Curie temperature (T_C) [41]. In Fig. 2d the post-annealed BM-26h-600 °C–N_2 sample holds a 8.2 K decrease in $T_C{}^{heating}$, compared with BM-26 h sample. The origin of ΔT_{hys} can be distinguished into intrinsic (e.g. electronic properties) and extrinsic contributions (e.g. dynamic sweeping rate) [42]. To get the intrinsic ΔT_{hys} and exclude extrinsic factors for the BM-26 h sample, in Fig. 2e different DSC sweeping rates (10, 7, 5, 2 K/min) have been chosen. From these curves an extrapolated value of $\Delta T_{hys} =$ 6.9 K is found at zero sweep rate, as shown in Fig. 2f. The data for the other BM samples derived by the same method are presented (dashed line) in Fig. 2c. Table 1 summarizes the changes in ΔT_{hys}, $T_C{}^{heating}$, $T_C{}^{cooling}$, $\langle T_C \rangle$ and ΔS_{tot} at different BM times.

The correlation between crystallite size and $T_C{}^{heating}$ was studied in Fig. 3a. With decreasing size from 86 nm (BM time of 1 h) to 28 nm (BM time of 26 h) $T_C{}^{heating}$ shows a decrease. This trend is in agreement with other reduced-dimension nanomaterials [43–46], for instance when in DyCuAl the crystallite size is reduced from 90 to 38 nm T_C reduces from 27 to 24 K [47] and in the $La_{0.6}Ca_{0.4}MnO_3$ nano-system T_C shifts from 270 to 258 K when the particle size decreases from 223 to 45 nm [48]. The reduced crystallite size also affects the hysteresis behavior in the form of thermal hysteresis [49], magnetic hysteresis [50] as well as stress hysteresis [51]. As shown in Fig. 3b, with decreasing crystallite size, ΔT_{hys} reduces from 14.9 K at a BM time of 0 h to 7.8 K at a BM time of 12 h, with a slight enhancement to 10.5 K at a BM time of 26 h.

3.3. Microstructural characterization

In order to investigate the microstructure evolution as a result of the nano-sizing SEM and HRTEM were performed, as shown in Fig. 4. In Fig. 4a, a SEM image of a collection of particles for the BM-16 h sample is shown. An obvious particle size distribution is observed with sizes ranging from several nanometer up to around 3 μm. Within some of the bigger particles several small nanoparticles (NPs) can be identified, as indicated inside the red boxes. Fig. 4b shows the HRTEM image of one isolated spherical particle with a diameter of about 35 nm for the BM-26 h sample, which is composed of a darker crystalline core and brighter amorphous shell. A fast Fourier transform (FFT) is applied which confirms that the core is single crystalline behavior. Fig. 4c indicates the inter-planar spacing is 0.20 nm. In Fig. 4d the bright-field HRTEM of one of the bigger particles (with a diameter of about 170 nm) from the same BM-26 h sample presents a similar shell layer. This shell layer is also found for the post-annealed particles (BM-26h-600 °C–N_2 sample) shown in Fig. S5b (Supplementary Information). The formation of an amorphous shell in NPs was also observed in nano Gd (inert-gas evaporation) [52], LaFeSi (pulsed laser deposition (PLD); spark ablation) [53,54], Heusler alloys (PLD) [55], manganese perovskite (sol-gel method) [48] and other oxide compounds (HEBM) [56]. By using a FFT and comparing the diffraction patterns we can evaluate the crystallite sizes within a polycrystalline particle. For instance in Fig. 4e, four single-domain areas have been indicated with crystallite sizes of 36.8, 40.0, 22.4 and 25.6 nm, respectively. The average crystallite size (31.2 nm) from HRTEM is in good agreement with the value estimated from XRD (28 nm). Fig. 4f and 4g show different electron diffraction patterns corresponding to single crystalline areas 4 and 2 in Fig. 4e, respectively. These two single crystalline areas have a

Table 1
Summary of thermal hysteresis (ΔT_{hys}), heating Curie temperature (T_C ^{heating}), cooling Curie temperature (T_C ^{cooling}), $\langle T_C \rangle$ and total entropy change (ΔS_{tot}).

BM time(h)	ΔT_{hys} (K)	T_C ^{heating} (K)	T_C ^{cooling} (K)	$<T_C>$ (K)	ΔS_{tot}(Jkg^{-1}K^{-1})
0	14.9	399.4	384.5	392.0	20.93
1	9.6	396.9	387.3	392.1	21.33
2	8.8	396.2	387.4	391.8	15.49
4	8.3	395.7	387.4	391.5	8.44
8	8.0	395.3	387.3	391.3	6.10
12	7.8	394.8	387.0	390.9	4.23
16	9.1	395.1	386.0	390.5	2.42
20	10.4	395.3	384.9	390.1	2.28
26	10.5	395.3	384.8	390.0	2.03
26 (+600°C-N_2)	8.7	386.5	377.8	382.1	2.86

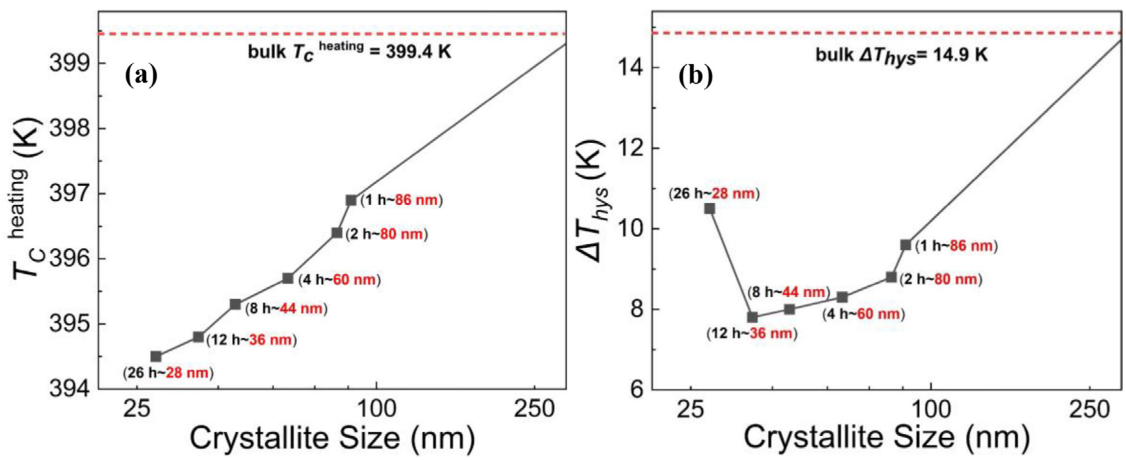

Fig. 3. (a) T_C ^{heating} and (b) ΔT_{hys} as a function of the average crystallite size. The horizontal axis is in log scale. The dashed lines reflect the bulk value obtained for zero BM time.

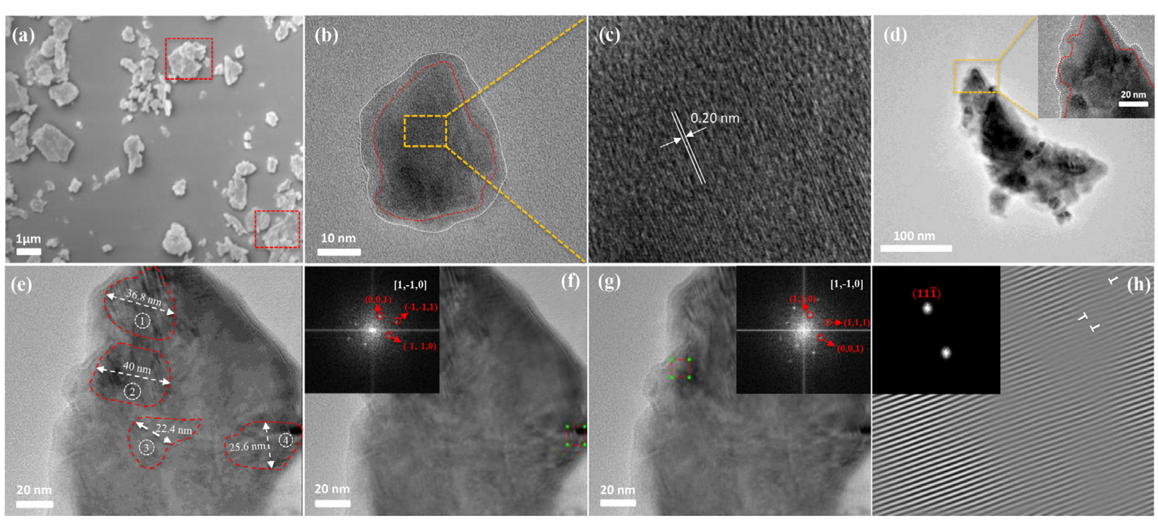

Fig. 4. (a) SEM image for the BM-16 h sample. (b) HRTEM image of isolated "core-shell" single domain particle for the BM-26 h sample. (c) Partial enlarged image collected from the yellow box in (b) together with the interplanar spacing. (d) Bright-field HRTEM image of one of the bigger particles in the BM-26 h sample. Inset demonstrates the shell layer. (e) Different single-crystalline areas within one particle. (f-g) Corresponding FFT patterns in the regions indicated by the red circles in (e) for the BM-26 h sample (region 4 in (f) and region 2 in (g)). (h) Corresponding IFFT pattern of (g) consisting of numerous dislocations marked with "T" along the (11$\bar{1}$) direction. (For interpretation of the references to colour in this figure legend, the reader is referred to the web version of this article.)

different crystallographic orientation. The diffraction patterns from the crystalline cores are consistent with a pure hexagonal structure along the [1,−1,0] zone axis, while the shell presents amorphous diffraction rings, as shown in Fig. S4 (Supplementary Information). The corresponding inverse fast Fourier transform (IFFT) image for the diffraction pattern of Fig. 4g is shown in Fig. 4h. In this figure some dislocation defects marked with "T" are observed along the (11$\bar{1}$) direction, which could be ascribed to severe plastic deformation during the HEBM process. The formation of such defects has also been observed in other HEBM nanomaterials [57,58]. The presence of dislocations may result in changes in structural, thermodynamic and magnetic properties. In contrast, widely distributed dislocations have not been observed in the corresponding IFFT image of the post-annealed sample (BM-26h-600 °C–N_2), as shown in Fig. S5e (Supplementary Information). This is expected to be a result of the annealing at a moderate temper-

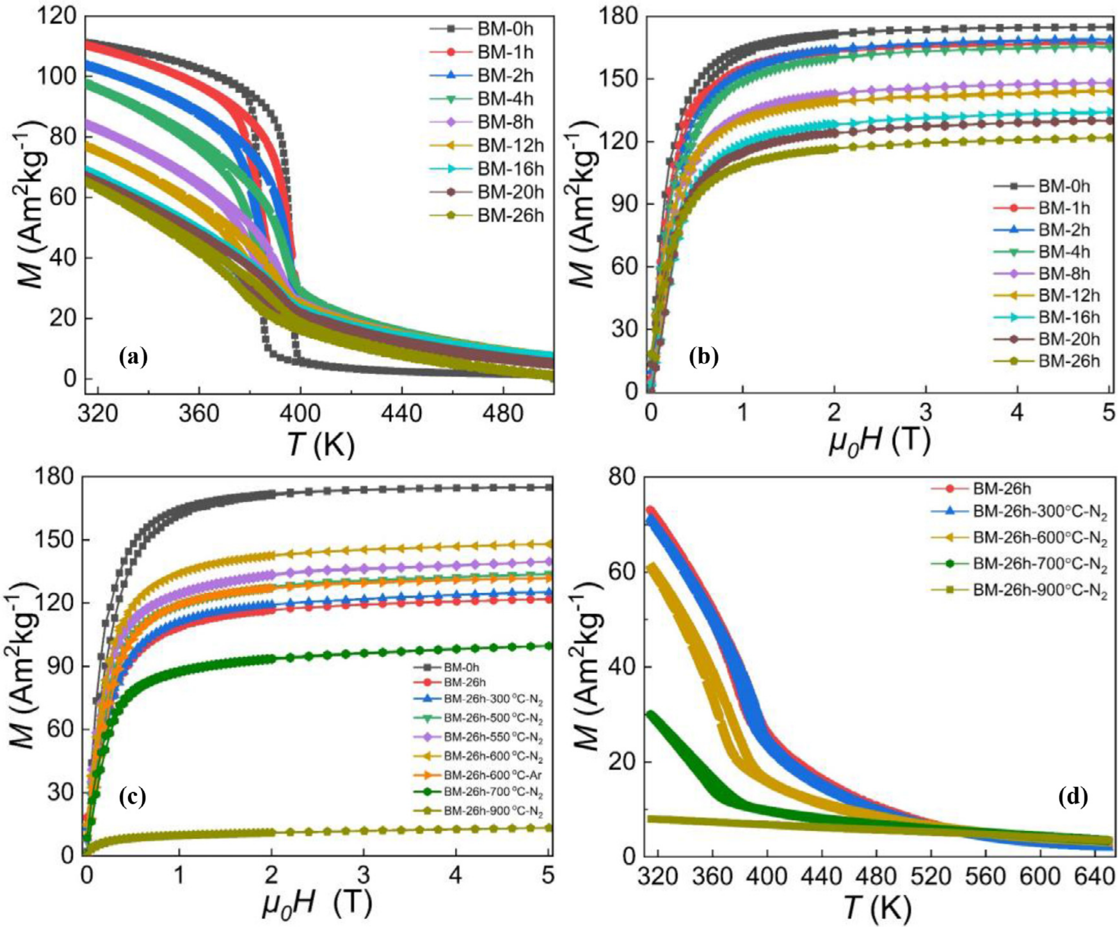

Fig. 5. (a) Temperature-dependent magnetization (*M-T*) curves at 1 T for $MnFeP_{0.45}Si_{0.55}$ samples with different BM times. (b) Isothermal field-dependent magnetization (*M-H*) curves at 5 K for samples with different BM times. (c) *M-H* curves at 5 K for the BM-0 h sample, the BM-26 h sample and post-annealed samples for BM-26 h after annealing at various temperatures and protective atmospheres. (d) *M-T* curves at 1 T for the BM-26 h sample and the corresponding post-treatment samples annealed in N_2 at different temperatures.

ature of 600 °C. To study the homogeneity of elemental distributions, energy-dispersive X-ray spectroscopy (EDS) mapping was performed in the HRTEM for the BM-26 h sample, as shown in Fig. S6 (Supplementary Information). It was found that the metal (Mn-Fe) and non-metal (P-Si) elements are homogeneously distributed in the matrix and that there is no obvious element segregation. The EDS mapping of sample BM-26h-600 °C–N_2 in Fig. S7 (Supplementary Information), also reveals the amount of doped nitrogen within one of the particles. For this sample annealing under a nitrogen environment results in a reduction in unit-cell volume (from 111.9 to 110.8 Å^3), indicating that N atoms enter the structure substitutionally [59]. Image analysis of Fig. S7 indicates that the particle shell contains a higher N concentration compared to the particle core, which may be attributed to the amorphous structure of the particle shell. N doping during annealing generally presents some positive effects [60–62], which is expected to be responsible for the optimization of magnetic properties discussed in the section below.

3.4. Magnetic properties

The change in crystallite size and microstructure upon nanosizing can also bring different magnetic properties with respect to the bulk behavior. For instance, from the *M-T* curves in Fig. 5a, it is observed that for increasing BM times the characteristic sharp FOMT for the bulk sample gradually disappears and that the transition area significantly broadens, which is expected to be related to the evolution of the particle size distribution. The isothermal *M-H* curves in Fig. 5b illustrate that the M_s decreases with increasing BM times, which can be ascribed to the gradual loss in long-range ferromagnetic order for smaller crystallite sizes. The gradual reduction in M_s with BM times is more pronounced after 4 h.

In Fig. 5c the saturation magnetization M_s at 5 K and 5 T decreases from 175 to 122 Am^{2}kg^{-1} for a BM time from 0 to 26 h, respectively. Interestingly, except for the bulk sample (BM-0 h), the 1st cycle magnetization and demagnetization curves almost overlap each other for all BM samples. This suggests that successive milling results in a decrease in magnetocrystalline anisotropy [41], which can be observed by the correspondence between the 1st cycle demagnetization and 2nd cycle magnetization process in subsequent *M-H* curves, presented in Fig. S8 (Supplementary Information). Because the decrease in M_s (~30%) will be detrimental to the MCE, we tried to recover this loss in M_s while maintaining the small crystallite size by N_2 gaseous nitriding. The approach was inspired by previous studies, which noticed an enhancement of the magnetic moments [62] and a refinement of the microstructure [60]. As exhibited in Fig. 5c, an optimal temperature window of 300–600 °C for annealing under N_2 atmosphere has been found where a clear enhancement in M_s is found for all post-annealed samples. For annealing temperatures above 600 °C the saturation magnetization M_s is reduced rapidly as the higher temperature leads to the formation of metal-nitride and the destruction of the hexagonal structure. Specifically, the M_s value for the

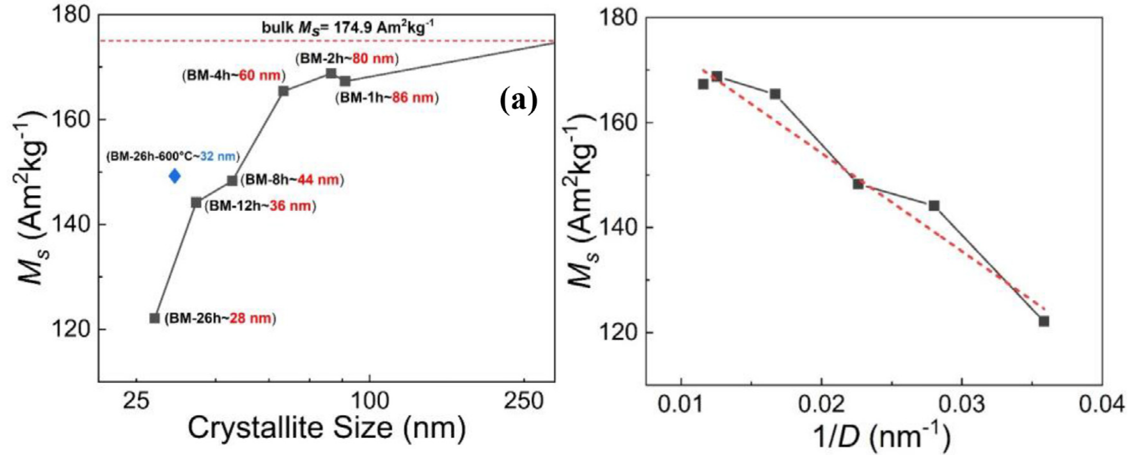

Fig. 6. (a) Saturation magnetization M_s measured in a field of 5 T at a temperature of 5 K as a function of the average crystallite size D (for different BM times). (b) Linear fitting between the M_s and $1/D$.

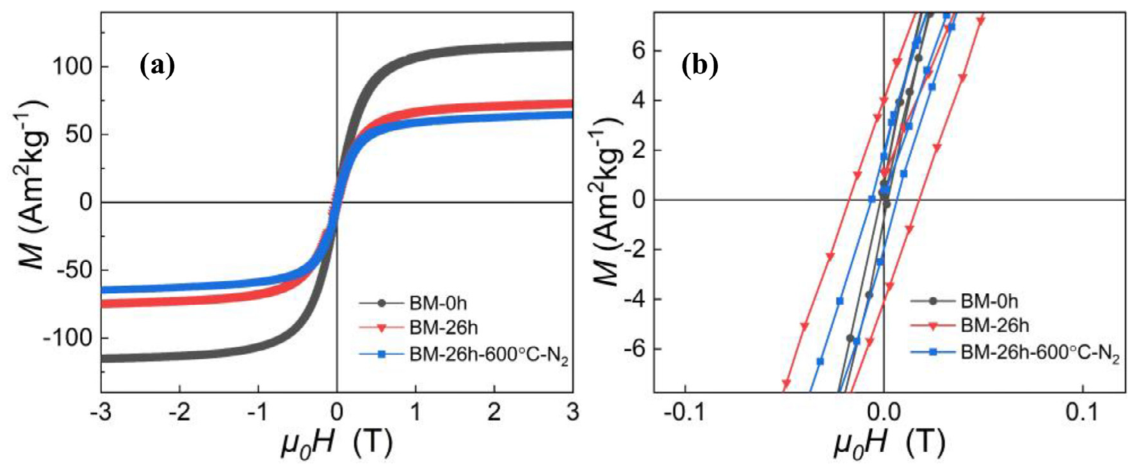

Fig. 7. (a) Magnetic hysteresis loops for the BM-0 h, BM-26 h and BM-26h-600 °C–N_2 samples at a temperature of 320 K. (b) Magnification of the magnetization loops of (a) near the origin.

BM-26h-600 °C–N_2 sample increased 22% from 127.5 to 147.9 (5 T) Am^2kg^{-1} in comparison to BM-26 h sample. However, for an annealing temperature above 600 °C (see the data for 700–900 °C in Fig. 5d), the transition is gradually suppressed due to the collapse of the hexagonal structure.

The relationship between M_s and the average crystallite size has been shown in Fig. 6a. It is found that M_s decreased continuously with decreasing crystallite size. This phenomenon has been widely investigated in different nanomaterials systems [63,64]. The decrease in M_s with the reduction in crystallite size might (partially) be ascribed to the existence of a so-called magnetic dead layer (MDL) on the surface [65], which means the surface shell becomes highly frustrated, leading to a reduced magnetic moment of the particle. The MDL is directly proportional to increased surface-volume ratio related to the decreased crystallite size. From HRTEM results in Fig. 4 an amorphous MDL has also been observed at the surface of the magnetic nanoparticles. Experimentally, the polarized small-angle neutron scattering (SANS) technique has proven that for maghemite/magnetite NPs a gradual decrease in magnetization can result from an enhanced tendency for spin canting near the surface [66,67]. As shown in Fig. 6b, the relationship between M_s and crystallite size can be well estimated by the following relation [63,68]:

$$M_s = M_{s0}\left(1 - \frac{6\gamma}{D}\right) \tag{1}$$

where M_s is the saturation magnetization of the nanomaterial, M_{s0} is the saturation magnetization of the bulk material, γ is the thickness of MDL (approximately 2–3 nm) and D is the average crystallite size.

The hysteresis loops in the FM state were obtained in Fig. 7a. As shown in Fig. 7b, the coercive field $\mu_0 H_c$ (negative intersection of the horizontal axis in the M-H curve for reducing field) for the BM-0 h, BM-26 h and BM-26h-600 °C–N_2 samples are 1.80, 17.6 and 6.50 mT, respectively. Compared to bulk $(Mn,Fe)_2(P,Si)$ and other soft magnetic MCMs [69], the BM-26 h sample exhibits a pronounced 10 times increase in coercive field $\mu_0 H_c$. The increase in $\mu_0 H_c$ with decreasing crystallite size D is also observed in some other polycrystalline materials where a $\mu_0 H_c \propto 1/D$ relation was reported [41,70]. The mechanically reduced crystallite size is expected to create more pinning sites, which are the main source for the enhanced value for $\mu_0 H_c$ [71]. As the mechanically reduced particle size can pin the magnetic domain wall movement, an additional driving force in the form of a higher applied magnetic field is needed to overcome the pinning of the magnetic domain walls before they start to move. The thickness of the magnetic domain wall (κ) in $(Mn,Fe)_2(P,Si)$ system can be estimated by following formula [72]:

$$\kappa = Na \tag{2}$$

$$\mathrm{N} = \sqrt{\pi^2 J S^2 / K a^3} \tag{3}$$

$$J = 3k_B T_c / 2zS(S+1) \tag{4}$$

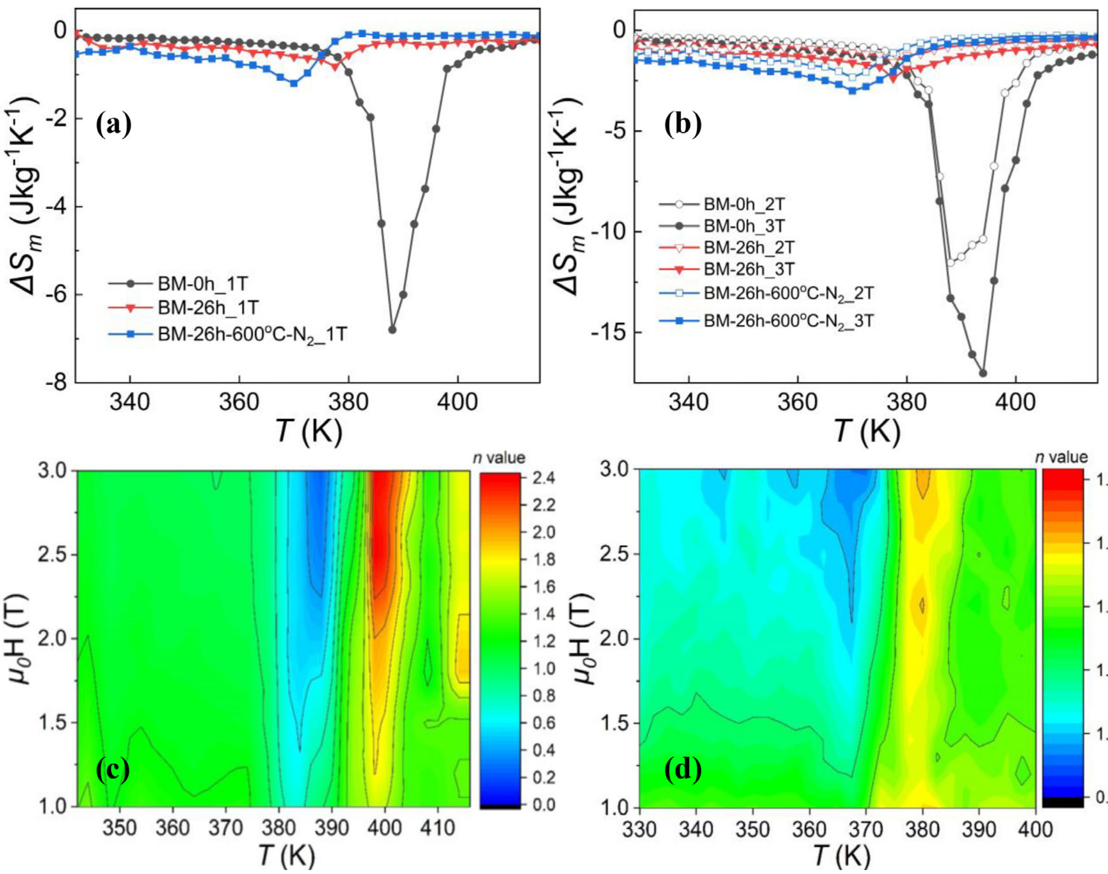

Fig. 8. Temperature dependence of ΔS_m for the BM-0 h, BM-26 h and BM-26h-600 °C–N_2 samples for a magnetic field change $\mu_0\Delta H$ of (a) 1 T and (b) 2 and 3 T (with respect to zero field); 2D contour plots of the field exponent n as a function of magnetic field and temperature for the (c) BM-0 h and (d) BM-26 h samples.

where N is the number of atomic planes contained within the magnetic domain wall; a is the effective lattice parameter ($a = \sqrt[3]{V/3}$ for an hexagonal system and V is the unit-cell volume); J is the exchange integral; S is the electron spins, which is deduced from $\mu_{eff} = 2\sqrt{S(S+1)}$ and $\mu_{\boldsymbol{eff}}$ is the effective (average) spin moment of the Mn and Fe atoms; K is the magneto-crystalline anisotropy constant (0.28×10^6 J/m^3 for $(Mn,Fe)_2(P,Si)$ system [73]); $k_{\boldsymbol{B}}$ is Boltzmann's constant; T_C is the Curie temperature and z is the number of nearest neighbors. The estimated magnetic domain wall thickness δ is 13 nm for the BM-26 h sample, which is of the same order of magnitude as the average crystallite size (28 nm). In addition, dislocations can also pin the motion of magnetic domain walls [74]. As a consequence it can cause a partial increase in μ_0H_c. For comparison, the BM-26h-600 °C–N_2 sample, which has a decreased dislocation density with respect to the BM-26 h sample shows a distinctly lower value for μ_0H_c, even though its value is still higher than that of the original BM-0 h bulk sample. In addition, the weak magnetic hysteresis in Fig. 7b is expected to be ascribed to the presence of a fraction of larger particles in the superparamagnetic material.

Based on the isothermal M-T curves presented in Fig. S9 (Supplementary Information), the magnetic field induced entropy change ΔS_m can be evaluated using the Maxwell relation $\Delta S_m = \int_0^H \left(\frac{\partial M}{\partial T}\right)_H dH$, which is associated with the configuration entropy arising from spin disorder [75]. Fig. 8a-b shows the negative heating ΔS_m values (conventional MCE) of three samples as a function of temperature for magnetic field changes $\mu_0\Delta H$ of 1, 2 and 3 T, respectively. For a field change of $\mu_0\Delta H$ = 1 T (characteristic for applications), the maximum value of $|\Delta S_m|$ decreases from 6.8 Jkg^{-1}K^{-1} for the original bulk BM-0 h sample to 0.8 Jkg^{-1}K^{-1} (88% loss) for the BM-26 h sample, which can be ascribed to a significant reduction in ΔM and a broadening of the phase transition. In comparison with the BM-26 h sample, the BM-26h-600 °C–N_2 sample shows an improvement in the maximum value of $|\Delta S_m|$ from 0.8 to 1.2 Jkg^{-1}K^{-1} (1.6 to 2.3 Jkg^{-1}K^{-1} for $\mu_0\Delta H$ =2 T). This is consistent with the increasing trend of the transformation peak in the DSC experiments and can originate from the synergistic effect of the reduced dislocation density and the nitrogen doping.

In Fig. 9a map of $|\Delta S_m|$ versus T_C is shown for some representative nano MCMs. For $La(Fe,Si)_{13}$, the other most promising MCMs, no data are reported, although several nano-compounds exist [53,54]. The post-annealed nano $MnFeP_{0.45}Si_{0.55}$ sample (BM-26h-600 °C–N_2) shows competitive $|\Delta S_m|$ values for field changes of 1 and 2 T, compared with the benchmark MCE material Gd in the form of nano-compounds.

Furthermore, ΔT_{ad} based on indirect measurements and the relative cooling power (RCP) used for evaluating the refrigeration capacity of a magnetic refrigerant can be obtained by expressions (5) [76] and (6) [48], respectively, as shown below:

$$\Delta T_{ad} \cong -\frac{T}{Cp}\Delta S_m(T,H) \tag{5}$$

$$RCP = |\Delta S_{m,max}|\delta T_{FWHM} \tag{6}$$

where C_p is zero-field specific heat and δT_{FWHM} is temperature difference between T_2 and T_1 at FWHM. All MCE parameters including T_{trans}, ΔS_m, ΔT_{ad}, RCP, D, and synthesis methods for our works and some classical nano MCMs are summarized in Table 2. Note that some nanomaterials focused on cryogenic magnetic refrigeration like Gd_2O_3 [77] and $GdNi_5$ [78] are not included due

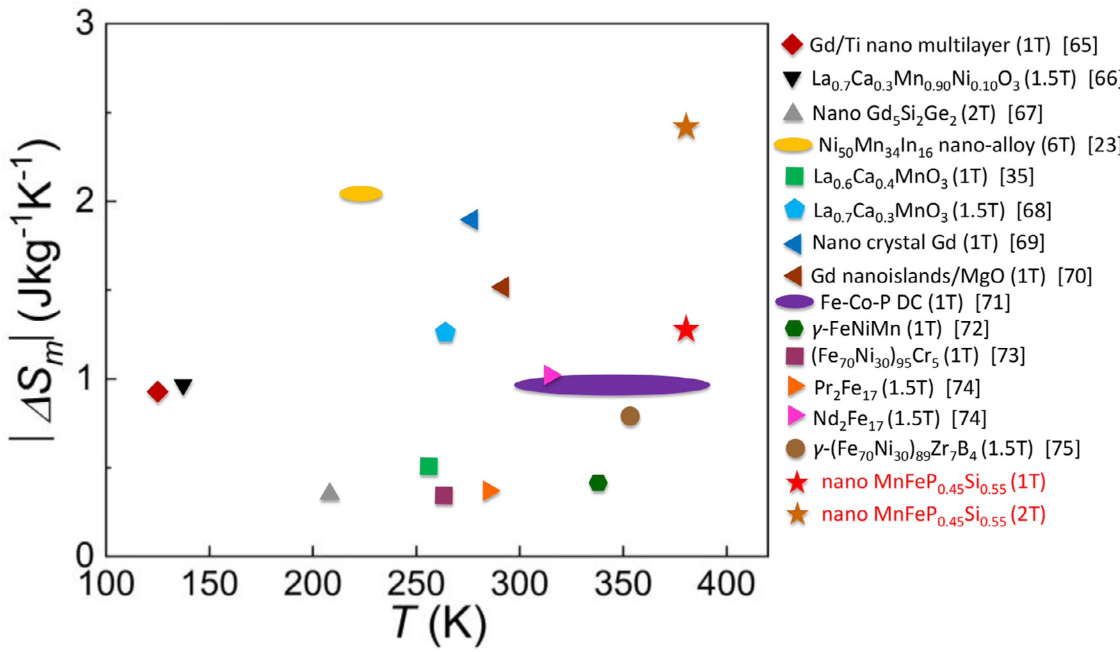

Fig. 9. Map of the absolute magnetic entropy change $|\Delta S_m|$ for different field changes $\mu_0 \Delta H$ as a function of the magnetic transition temperature for nano MCMs [35,48,79-89]. The stars correspond to the present data for the BM-26h-600 °C–N_2 sample.

Table 2
Transition temperature (T_{trans}), magnetic entropy change $|\Delta S_m|$, adiabatic temperature change ΔT_{ad}, *RCP*, crystallite size *D* and synthesis method for selected nano MCMs reported in the literature.

Nano MCMs system	T_{trans}(K)	$\|\Delta S_m\|$(Jkg^{-1}K^{-1})	ΔT_{ad}(K)	*RCP*(Jkg^{-1})	*D* (nm)	Synthesismethods	References
Pr_2Fe_{17} and Nd_2Fe_{17}	∼285; ∼337	0.6 (1.5 T); 1 (1.5 T)	–	60 (1.5 T) 118 (1.5 T)	11;11	BM 40h	[88]
γ-FeNiMn	340	0.41 (1 T)	–	78 (1 T)	17	BM 10h	[86]
$(Fe_{70}Ni_{30})_{95}Cr_5$	258	∼0.3 (1 T)	–	77 (1 T)	13	BM method	[87]
Fe-Co-P DC	300–390	0.907 (1 T)	0.77 (1 T)	52 (1 T)	<100	electrodeposition	[85]
γ-$(Fe_{70}Ni_{30})_{89}Zr_7B_4$	353	0.7 (1.5 T)	–	65 (1.5 T)	20	BM method	[89]
Nano Gd	–	∼0.4 (0.1 T)	–	–	12	alkalide reduction	[93]
Gd nanoislands/MgO	296.2	∼1.5 (1 T)	–	–	∼131	solid-state dewetting	[84]
$La_{0.7}Ca_{0.3}MnO_3$	266	1.2 (1.5 T)	–	44 (1.5 T)	65	sol-gel method	[82]
$La_{0.7}Ca_{0.3}Mn_{0.9}Ni_{0.1}O_3$	145	0.95 (1.5 T)	–	–	15	BM method	[80]
$La_{0.6}Ca_{0.4}MnO_3$	258	0.6 (1 T)	–	50 (1 T)	45	sol-gel method	[48]
Nano crystal Gd	285.6	∼1.8 (1 T)	–	–	12	inert gas condensation	[83]
Gd/Ti nano multilayer	130	∼0.9 (1 T)	–	–	–	sputtering deposition	[79]
Nano $Gd_5Si_2Ge_2$	∼225	0.45 (2 T)	–	–	85	BM method	[81]
Nano $LaFe_{11.5}Si_{1.5}$	200–340	–	–	–	∼6.5	spark ablation	[54]
$Ni_{50}Mn_{34}In_{16}$ nano-alloy	226–241	2 (6 T)	–	150 (6 T)	150	BM method	[35]
$MnFeP_{0.45}Si_{0.55}$ BM-26h-600 °C–N_2	∼382	1.2 (1 T); 2.4 (2 T)	0.9 (1 T) 1.74 (2 T)	29 (1 T) 77 (2 T)	31.6	BM 26h	this work

to their extreme low working temperature (< 30 K), even though they present a relatively high ΔS_m at high field changes.

In addition, to distinguish the FOMT or SOMT nature of the phase transition, Arrott plots ($\mu_0 H/M$ versus M^2) were constructed for the BM-0 h, BM-26 h and BM-26h-600 °C–N_2 samples. The Arrott plots were made from the isothermal *M-H* curves presented in Fig. S9 (Supplementary Information), assuming a demagnetization factor of $N = 1/3$ (assuming an equiaxed powder sample volume). Although the BM-0 h sample represents clear FOMT characteristics (with a "S-shaped" curve as predicted by the Banerjee criterion), the other two samples appear to be of SOMT type, which is in conflict with the observed hysteresis. Hence, the recently proposed field exponent *n* for the magnetic entropy change [90] is applied to further identify the nature of the magnetic transition. This field exponent is defined as:

$$n(T, H) = \frac{d\ln|\Delta S_M|}{d\ln H} \quad (7)$$

2D-plots of exponent $n(T,H)$ as a function of temperature *T* and applied magnetic field *H* have been shown in Fig. 8c-d for the BM-0 h and BM-26 h samples. Close to the magnetic transition the *n* value peaks at a value above the value obtained for the paramagnetic state at higher temperature, a characteristic feature for a FOMT [91,92]. We therefore conclude that: (1) the BM-0 h sample is a strong FOMT ($n > 2$) in agreement with the Banerjee criterion in the Arrott plot and (2) the BM-26 h sample shows a weak FOMT, rather than SOMT.

3.5. Mössbauer spectra and superparamagnetic particles

When the dimension of a magnetic particle is below a certain size (e.g. 50 nm) it will be single magnetic domain and presents superparamagnetism (SPM) above the so-called blocking temperature T_B [94]. As mentioned, the HRTEM results (Fig. 4b) show individual nanoscale crystallites, which based on their size are ex-

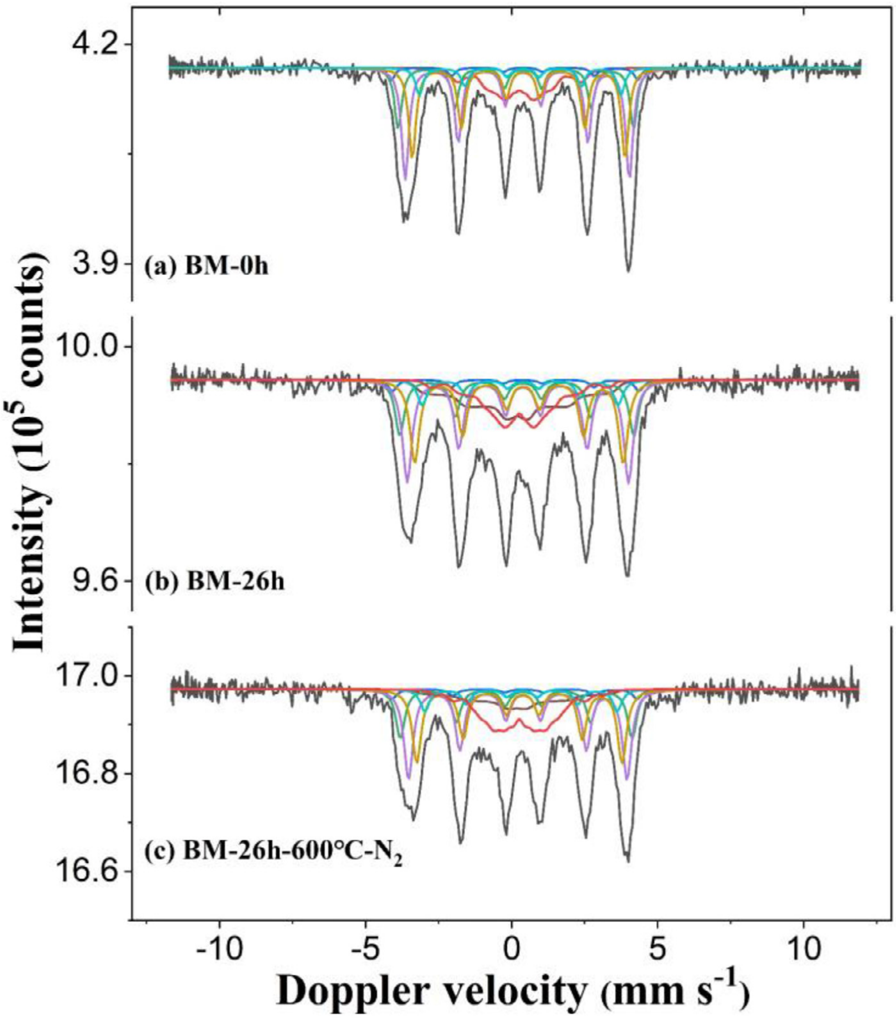

Fig. 10. Mössbauer spectra for the (a) BM-0 h, (b) BM-26 h and (c) BM-26h-600 °C–N_2 samples recorded at 4.2 K. Note that the five middle sextets (blue, green, purple, dark yellow, cyan) correspond to the FM components of the main phase, the red curves correspond to the $(Mn,Fe)_3Si$ impurity phase, the middle brown curves correspond to the SPP phase and the black curves represent the sum. (For interpretation of the references to colour in this figure legend, the reader is referred to the web version of this article.)

Table 3
Mössbauer fit parameters for the BM-0 h, BM-26 h and BM-26h-600 °C–N_2 samples at 4.2 K. (F- ferromagnetic phase; IM- impurity phase $(Mn,Fe)_3Si$; SPP- superparamagnetic particles).

Sample	*IS* (mms^{-1})	*QS* (mms^{-1})	Hyperfine field (T)	Γ (mms^{-1})	Phase	Spectral contribution (%)
BM-0h	0.30(1)	−0.19(1)	23.6(1)	0.30(1)	F	85(3)
	0.27(2)	-	8.8(5)	0.30(1)	IM	15(3)
BM-26h	0.31(1)	−0.17(1)	23.3(1)	0.39(1)	F	67(3)
	0.27(2)	-	8.8(5)	0.30(1)	IM	15(3)
	0.19(2)	-	12.0(5)	0.39(1)	SPP	18(3)
BM-26h-	0.31(1)	−0.17(1)	23.0(1)	0.37(1)	F	71(3)
600 °C-N_2	0.27(2)	-	8.8(5)	0.30(1)	IM	19(3)
	0.17(2)	-	10.9(5)	0.37(1)	SPP	10(3)

pected to behave as superparamagnetic particles (SPP). Because Mössbauer spectroscopy is very sensitive to the magnetic properties of nanoscale particles, it is an excellent technique to provide more details about SPM in $(Mn,Fe)_2(P,Si)$-based nano MCMs. The Mössbauer spectra at 4.2 K for the BM0h, BM-26 h and BM-26h-600 °C–N_2 samples are shown in Fig. 10. The fitted hyperfine parameters include the average isomer shift (δ), the average quadrupole splitting (*QS*), the hyperfine field and linewidth (Γ) and are presented in Table 3. Obviously, the values of δ and *QS* for the main phase remain almost unchanged, but the reduced hyperfine fields for the BM samples indicate a decrease in Fe moment. The line width Γ is enhanced with increasing BM time, reflecting the development of a wide distribution of magnetic fields acting on the Fe nuclei [95]. The five sets of sextets observed in Fig. 10 correspond to five types of chemical coordination environment of Fe. Simultaneously, the phase fraction of the SPP for the BM samples of 18% for the BM-26 h sample and 10% for the BM-26h-600 °C–N_2 sample is clearly enhanced. In Fig. 10a typical ferromagnetic sextet (middle brown curve) appears due to the existence of collective magnetic interactions below T_B [96]. For comparison, in Fig. S10

(Supplementary Information) the hyperfine lines at 130 K become asymmetrically broadened and a single line appears. These are fundamental features of SPM for nanoscale particles, as seen in the Mössbauer spectra [56,95,97,98].

This phenomenon can be understood by considering the SPM relaxation time estimated by the Néel–Brown–Arrhenius expression [99]:

$$\tau_R = \tau_0 \exp\left(KV/k_B T\right) \tag{8}$$

where τ_R is the relaxation time of the magnetization vector in a particle, τ_0 is a characteristic time constant that is roughly equal to 1×10^{-9} s, K is the magnetic anisotropy constant, V is volume of the crystallite and $k_B T$ corresponds to the thermal energy. If $\tau_R < \tau_L$ then a superparamagnetic doublet/singlet will appear, where $\tau_L \approx 10^{-8}$ - 10^{-9} s is the Larmor precession time of the nucleus. For $\tau_R > \tau_L$ a minor sextet structure is observed, while for the intermediate range with $\tau_R \approx \tau_L$ complex spectra with broadened lines are found. Other evidence for the presence of SPM can be found in the *M-T* curves at 0.1 T for ZFC-FC conditions, as presented in Fig. S11 (Supplementary Information) for the BM-26 h and BM-26h-600 °C–N_2 samples. Typical magnetization divergences were observed, which are characteristic of SPM in nanoscale particles [100]. The blocking temperature T_B (at 0.1 T) is determined to be 72 and 61 K for the BM-26 h and BM-26h-600 °C–N_2 samples, respectively. Annealing is found to reduce T_B, which in agreement with observations for other nano-systems [101]. The critical diameter for single magnetic domain behavior (D_{sd}) for $(Mn,Fe)_2(P,Si)$-based compounds can be estimated by [72]:

$$D_{sd} = 2R_{sd} \cong 9\gamma_w / k_d \tag{9}$$

where R_{sd} is the single domain radius, $\gamma_w = 2\sqrt{AK}$ is the surface energy of a Bloch wall and $k_d = J_s^2/2\mu_0 = \frac{1}{2}\mu_0 M_s^2$ is the stray field energy (J_s is the saturation magnetization). Thus D_{sd} can be deduced from (9):

$$D_{sd} = 36\sqrt{AK}/\mu_0 M_S^2 \tag{10}$$

$$A = nJ_{ex}S^2/a \tag{11}$$

where A is the exchange stiffness constant, n is the number of atoms in one unit cell, J_{ex} is the exchange integral, S is the spin, a is the lattice parameter, K is the magnetocrystalline anisotropy constant, μ_0 is the permeability of vacuum and M_s is the saturation magnetization. The value for D_{sd} is estimated to be 29.8 nm for $(Mn,Fe)_2(P,Si)$-based compounds. This is in accordance with our XRD results where the crystallite size was estimated to be about 28 nm for the BM-26 h sample and the HRTEM results of Fig. 4e with an average crystallite size of 31.2 nm.

4. Conclusions

In summary, we have systematically studied the crystalline structure, thermodynamic-, microstructure- and magnetic properties in $(Mn,Fe)_2(P,Si)$-based nano MCMs derived from bulk alloys by XRD, DSC, HRTEM, SQUID and Mössbauer spectra. The change in crystallite size as a result of the HEBM process is found to be responsible for changes in T_C, ΔT_{hys}, ΔS_{tot} and the magnetization. Nano-sizing MCMs can be used to regulate T_C and $\Delta T_{hys,}$ similarly as with certain doping elements, tuning composition, optimizing annealing conditions and adjusting physical pressure. An efficient sample treatment after the HEBM process was adopted, which consists of annealing in a temperature window of 300 - 600 °C with gaseous nitriding. Even though the $|\Delta S_m|$ of the bulk material (6.8 $Jkg^{-1}K^{-1}$ with $\mu_0\Delta H$ =1 T) is found to be significantly reduced by nanostructuring, the nitriding procedure was found to result in a significant recovery of the lost magnetization with an improvement in $|\Delta S_m|$ ($\mu_0 \Delta H$ = 1 T) from 0.8 to 1.2 $Jkg^{-1}K^{-1}$. During this procedure the crystallite size remained almost constant, which demonstrates competitive MCE characteristics among the reported nano MCMs systems. A core-shell type nanostructure, with a crystalline core and an atomically disordered shell, has been observed for the first time in $(Mn,Fe)_2(P,Si)$-based nano MCMs. The existence of superparamagnetic NPs has been proved by HRTEM, Mössbauer spectroscopy and magnetic measurement. Our study provides essential insight in $(Mn,Fe)_2(P,Si)$-based nano MCMs and opens the possibility to further develop its potential for future applications in the field of microrefrigerators, ferrofluids, nanocomposites, heterogeneous catalysis and magnetic hyperthermia.

Declaration of Competing Interest

The authors declare that they have no known competing financial interests or personal relationships that could have appeared to influence the work reported in this paper.

Acknowledgments

The authors thank Anton Lefering, Bert Zwart, Frans Ooms and Michel Steenvoorden for their technical assistance. This work was sponsored by NWO in the domain of the Applied and Engineering Sciences (AES) program. Support from the EIT Climate KIC project “Local, magnetocaloric power conversion opportunities for Cities” (ID 210045) is acknowledged. Fengqi Zhang gratefully acknowledges financial support from the China Scholarship Council. This work was partially carried out in the framework of the Joint Lab BiBer.

Supplementary materials

Supplementary material associated with this article can be found, in the online version, at doi:10.1016/j.actamat.2021.117532.

References

[1] V.K. Pecharsky, K.A. Gschneidner, Giant magnetocaloric effect in Gd5(Si2Ge2), Phys. Rev. Lett. 78 (23) (1997) 4494–4497.
[2] O. Tegus, E. Brück, K.H.J. Buschow, F.R. de Boer, Transition-metal-based magnetic refrigerants for room-temperature applications, Nature 415 (6868) (2002) 150–152.
[3] N.T. Trung, Z.Q. Ou, T.J. Gortenmulder, O. Tegus, K.H.J. Buschow, E. Brück, Tunable thermal hysteresis in MnFe(P,Ge) compounds, Appl. Phys. Lett. 94 (10) (2009) 1–3.
[4] F. Guillou, G. Porcari, H. Yibole, N. van Dijk, E. Brück, Taming the first-order transition in giant magnetocaloric materials, Adv. Mater. 26 (17) (2014) 2671–2675.
[5] F.X. Hu, B.G. Shen, J.R. Sun, Z.H. Cheng, G.H. Rao, X.X. Zhang, Influence of negative lattice expansion and metamagnetic transition on magnetic entropy change in the compound LaFe11.4Si1.6, Appl. Phys. Lett. 78 (23) (2001) 3675–3677.
[6] A. Planes, L. Manosa, M. Acet, Magnetocaloric effect and its relation to shape-memory properties in ferromagnetic Heusler alloys, J. Phys.-Condens. Mat. 21 (23) (2009) 1–29.
[7] A. Chirkova, K.P. Skokov, L. Schultz, N.V. Baranov, O. Gutfleisch, T.G. Woodcock, Giant adiabatic temperature change in FeRh alloys evidenced by direct measurements under cyclic conditions, Acta Mater. 106 (2016) 15–21.
[8] P.A.E. Murgatroyd, K. Routledge, S. Durdy, M.W. Gaultois, T.W. Surta, M.S. Dyer, J.B. Claridge, S.N. Savvin, D. Pelloquin, S. Hebert, J. Alaria, Chemically controllable magnetic transition temperature and magneto-elastic coupling in MnZnSb compounds, Adv. Funct. Mater. 31 (17) (2021) 1–9.
[9] J. Liu, Y.Y. Gong, Y.R. You, X.M. You, B.W. Huang, X.F. Miao, G.Z. Xu, F. Xu, E. Brück, Giant reversible magnetocaloric effect in MnNiGe-based materials: minimizing thermal hysteresis via crystallographic compatibility modulation, Acta Mater. 174 (2019) 450–458.
[10] T. Gottschall, K.P. Skokov, M. Fries, A. Taubel, I. Radulov, F. Scheibel, D. Benke, S. Riegg, O. Gutfleisch, Making a cool choice: the materials library of magnetic refrigeration, Adv. Energy Mater. 9 (34) (2019) 1–13.
[11] J.W. Lai, B.W. Huang, X.F. Miao, N.V. Thang, X.M. You, M. Maschek, L. van Eijck, D.C. Zeng, N. van Dijk, E. Brück, Combined effect of annealing temperature and vanadium substitution for mangetocaloric Mn1.2-xVxFe0.75P0.5Si0.5 alloys, J. Alloy Compd. 803 (2019) 671–677.
[12] J.W. Lai, X. Tang, H. Sepehri-Amin, K. Hono, Tuning transition temperature of magnetocaloric Mn1.8Fe0.2(P0.59Si0.41)x alloys for cryogenic magnetic refrigeration, Scr. Mater. 183 (2020) 127–132.

[13] N.H. Dung, Z.Q. Ou, L. Caron, L. Zhang, D.T.C. Thanh, G.A. de Wijs, R.A. de Groot, K.H.J. Buschow, E. Bruck, Mixed magnetism for refrigeration and energy conversion, Adv. Energy Mater. 1 (6) (2011) 1215–1219.
[14] X.F. Miao, L. Caron, P. Roy, N.H. Dung, L. Zhang, W.A. Kockelmann, R.A. de Groot, N.H. van Dijk, E. Brück, Tuning the phase transition in transition-metal-based magnetocaloric compounds, Phys. Rev. B 89 (17) (2014) 1–6.
[15] H. Yibole, F. Guillou, L. Caron, E. Jimenez, F.M.F. de Groot, P. Roy, R. de Groot, N.H. van Dijk, E. Brück, Moment evolution across the ferromagnetic phase transition of giant magnetocaloric (Mn,Fe)2(P,Si,B) compounds, Phys. Rev. B 91 (1) (2015) 1–10.
[16] M.F.J. Boeije, P. Roy, F. Guillou, H. Yibole, X.F. Miao, L. Caron, D. Banerjee, N.H. van Dijk, R.A. de Groot, E. Bruck, Efficient room-temperature cooling with magnets, Chem. Mater. 28 (14) (2016) 4901–4905.
[17] V. Chaudhary, Z. Wang, A. Ray, I. Sridhar, R.V. Ramanujan, Self pumping magnetic cooling, J. Phys. D 50 (3) (2017) 03LT03.
[18] D.J. Silva, B.D. Bordalo, A.M. Pereira, J. Ventura, J.P. Araujo, Solid state magnetic refrigerator, Appl. Energy 93 (2012) 570–574.
[19] K. Klinar, M.M. Rojo, Z. Kutnjak, A. Kitanovski, Toward a solid-state thermal diode for room-temperature magnetocaloric energy conversion, J. Appl. Phys. 127 (23) (2020) 234101.
[20] A. Kitanovski, P.W. Egolf, Innovative ideas for future research on magnetocaloric technologies, Int. J. Refrig. 33 (3) (2010) 449–464.
[21] S. Pal, A. Datta, S. Sen, A. Mukhopdhyay, K. Bandopadhyay, R. Ganguly, Characterization of a ferrofluid-based thermomagnetic pump for microfluidic applications, J. Magn. Magn. Mater. 323 (21) (2011) 2701–2709.
[22] D.N. Ba, L. Becerra, N. Casaretto, J.E. Duvauchelle, M. Marangolo, S. Ahmim, M. Almanza, M. LoBue, Magnetocaloric gadolinium thick films for energy harvesting applications, AIP Adv. 10 (3) (2020) 1–4.
[23] D.N. Ba, Y.L. Zheng, L. Becerra, M. Marangolo, M. Almanza, M. LoBue, Magnetocaloric effect in flexible, free-standing gadolinium thick films for energy conversion applications, Phys. Rev. Appl. 15 (6) (2021) 064045.
[24] X.L. Liu, Y.F. Zhang, Y.Y. Wang, W.J. Zhu, G.L. Li, X.W. Ma, Y.H. Zhang, S.Z. Chen, S. Tiwari, K.J. Shi, S.W. Zhang, H.M. Fan, Y.X. Zhao, X.J. Liang, Comprehensive understanding of magnetic hyperthermia for improving antitumor therapeutic efficacy, Theranostics 10 (8) (2020) 3793–3815.
[25] J.B. Li, Y. Qu, J. Ren, W.Z. Yuan, D.L. Shi, Magnetocaloric effect in magnetothermally-responsive nanocarriers for hyperthermia-triggered drug release, Nanotechnology 23 (50) (2012) 505706.
[26] T. Yadav, R. Yadav, D. Singh, Mechanical milling: a top down approach for the synthesis of nanomaterials and nanocomposites, Nanosci. Nanotechnol. 2 (3) (2012) 22–48.
[27] F. Guillou, H. Yibole, Z.Q. Ou, E. Brück, O. Tegus, Large recalescence-like event at the first cooling across the magnetic transition of (Mn,Fe)2(P,Si) magnetocaloric materials, Scr. Mater. 160 (2019) 81–85.
[28] H.M. Rietveld, A profile refinement method for nuclear and magnetic structures, J. Appl. Crystallogr. 2 (1969) 65–71.
[29] R.P. Hermann, O. Tegus, E. Brück, K.H.J. Buschow, F.R. de Boer, G.J. Long, F. Grandjean, Mossbauer spectral study of the magnetocaloric FeMnP1-xAsx compounds, Phys. Rev. B 70 (21) (2004) 1–9.
[30] X.F. Miao, S.Y. Hu, F. Xu, E. Bruck, Overview of magnetoelastic coupling in (Mn, Fe)2(P, Si)-type magnetocaloric materials, Rare Metals 37 (9) (2018) 723–733.
[31] U. Holzwarth, N. Gibson, The Scherrer equation versus the 'Debye-Scherrer equation, Nat. Nanotechnol. 6 (9) (2011) 534.
[32] G.S. Song, M. Staiger, M. Kral, Some new characteristics of the strengthening phase in beta-phase magnesium-lithium alloys containing aluminum and beryllium, Mat. Sci. Eng. A 371 (1–2) (2004) 371–376.
[33] H.G. Jiang, M. Ruhle, E.J. Lavernia, On the applicability of the x-ray diffraction line profile analysis in extracting grain size and microstrain in nanocrystalline materials, J. Mater. Res. 14 (2) (1999) 549–559.
[34] Z. Zhang, F. Zhou, E.J. Lavernia, On the analysis of grain size in bulk nanocrystalline materials via X-ray diffraction, Metall. Mater. Trans. A34a(6) (2003) 1349–1355.
[35] V. Sanchez-Alarcos, V. Recarte, J.I. Perez-Landazabal, S. Larumbe, R. Caballero-Flores, I. Unzueta, J.A. Garcia, F. Plazaola, J.A. Rodriguez-Velamazan, Mechanically induced disorder and crystallization process in Ni-Mn-In ball-milled alloys, J. Alloy Compd. 689 (2016) 983–991.
[36] D. Wu, H. Kahn, J.C. Dalton, G.M. Michal, F. Ernst, A.H. Heuer, Orientation dependence of nitrogen supersaturation in austenitic stainless steel during low-temperature gas-phase nitriding, Acta Mater. 79 (2014) 339–350.
[37] Y.Z. Li, Y.B. Li, Y.M. Sun, B. Butz, K. Yan, A.L. Koh, J. Zhao, A. Pei, Y. Cui, Revealing nanoscale passivation and corrosion mechanisms of reactive battery materials in gas environments, Nano Lett. 17 (8) (2017) 5171–5178.
[38] M. Fries, L. Pfeuffer, E. Bruder, T. Gottschall, S. Ener, L.V.S. Diop, T. Grob, K.P. Skokov, O. Gutfleisch, Microstructural and magnetic properties of Mn-Fe-P-Si (Fe2P-type) magnetocaloric compounds, Acta Mater. 132 (2017) 222–229.
[39] F.A. Mohamed, A dislocation model for the minimum grain size obtainable by milling, Acta Mater. 51 (14) (2003) 4107–4119.
[40] Z. Gercsi, E.K. Delczeg-Czirjak, L. Vitos, A.S. Wills, A. Daoud-Aladine, K.G. Sandeman, Magnetoelastic effects in doped Fe2P, Phys. Rev. B 88 (2) (2013) 024417.
[41] B.D. Cullity, C.D. Grahem, Introduction to Magnetic Materials, 2008.
[42] O. Gutfleisch, T. Gottschall, M. Fries, D. Benke, I. Radulov, K.P. Skokov, H. Wende, M. Gruner, M. Acet, P. Entel, M. Farle, Mastering hysteresis in magnetocaloric materials, Philos. Trans. R. Soc. A 374 (2074) (2016) 1–21.
[43] D. Michels, C.E. Krill, R. Birringer, Grain-size-dependent Curie transition in nanocrystalline Gd: the influence of interface stress, J. Magn. Magn. Mater. 250 (1–3) (2002) 203–211.
[44] A.S. Bolokang, M.J. Phasha, Thermal analysis on the curie temperature of nanocrystalline Ni produced by ball milling, Adv. Powder Technol. 22 (4) (2011) 518–521.
[45] Z. Zhao, V. Buscaglia, M. Viviani, M.T. Buscaglia, L. Mitoseriu, A. Testino, M. Nygren, M. Johnsson, P. Nanni, Grain-size effects on the ferroelectric behavior of dense nanocrystalline BaTiO3 ceramics, Phys. Rev. B 70 (2) (2004) 1–8.
[46] A.F. Manchon-Gordon, R. Lopez-Martin, A. Vidal-Crespo, J.J. Ipus, J.S. Blazquez, C.F. Conde, A. Conde, Distribution of transition temperatures in magnetic transformations: sources, effects and procedures to extract information from experimental data, Metals-Basel 10 (2) (2020) 1–23.
[47] Q.Y. Dong, B.G. Shen, S.L. He, H.W. Jiang, W. Zheng, J.R. Sun, Effect of crystal grain dimension on the magnetic properties and magnetocaloric effects in DyCuAl compound, J. Nanosci. Nanotechnol. 12 (2) (2012) 1040–1043.
[48] V.M. Andrade, R.J.C. Vivas, S.S. Pedro, J.C.G. Tedesco, A.L. Rossi, A.A. Coelho, D.L. Rocco, M.S. Reis, Magnetic and magnetocaloric properties of La0.6Ca0.4MnO3 tunable by particle size and dimensionality, Acta Mater. 102 (2016) 49–55.
[49] T. Gottschall, D. Benke, M. Fries, A. Taubel, I.A. Radulov, K.P. Skokov, O. Gutfleisch, A matter of size and stress: understanding the first-order transition in materials for solid-state refrigeration, Adv. Funct. Mater. 27 (32) (2017) 1–6.
[50] F.X. Hu, L. Chen, J. Wang, L.F. Bao, J.R. Sun, B.G. Shen, Particle size dependent hysteresis loss in La0.7Ce0.3Fe11.6Si1.4C0.2 first-order systems, Appl. Phys. Lett. 100 (7) (2012) 1–4.
[51] X.B. Shi, F.M. Guo, J.S. Zhang, H.L. Ding, L.S. Cui, Grain size effect on stress hysteresis of nanocrystalline NiTi alloys, J. Alloy Compd. 688 (2016) 62–68.
[52] I. Aruna, B.R. Mehta, L.K. Malhotra, S.M. Shivaprasad, Stability and hydrogenation of "bare" gadolinium nanoparticles, Adv. Funct. Mater. 15 (1) (2005) 131–137.
[53] N.R. Checca, W.S. Torres, R.J. Caraballo-Vivas, M.A.V. Heringer, D.R. Sanchez, A. Rossi, M.S. Reis, D.L. Rocco, Off-stoichiometry LaFe5Six cubic phase induced by the reduced size of the nanoparticles produced by pulsed laser deposition, J. Alloy Compd. 803 (2019) 417–423.
[54] J.C. Feng, R. Geutjens, N.V. Thang, J.J. Li, X.A. Guo, A. Keri, S. Basak, G. Galbacs, G. Biskos, H. Nirschl, H.W. Zandbergen, E. Bruck, A. Schmidt-Ott, Magnetic phase transition in spark-produced ternary LaFeSi nanoalloys, ACS Appl. Mater. Inter. 10 (7) (2018) 6073–6078.
[55] N.R. Checca, R.J. Caraballo-Vivas, A.A. Coelho, A. Rossi, N.M. Fortunato, F. Mohseni, J.N. Goncalves, J.S. Amaral, D.L. Rocco, M.S. Reis, Experimental realisation of off-stoichiometric Fe-Mn-Si full Heusler alloy with hexagonal crystal structure by pulsed laser deposition, Mater. Des. 143 (2018) 268–273.
[56] V. Sepelak, I. Bergmann, A. Feldhoff, P. Heitjans, F. Krumeich, D. Menzel, F.J. Litterst, S.J. Campbell, K.D. Becker, Nanocrystalline nickel ferrite, NiFe2O4: mechanosynthesis, nonequilibrium cation distribution, canted spin arrangement, and magnetic behavior, J. Phys. Chem. C 111 (13) (2007) 5026–5033.
[57] F.L. Zhang, C.Y. Wang, M. Zhu, Nanostructured WC/Co composite powder prepared by high energy ball milling, Scr. Mater 49 (11) (2003) 1123–1128.
[58] D. Raabe, S. Ohsaki, K. Hono, Mechanical alloying and amorphization in Cu-Nb-Ag in situ composite wires studied by transmission electron microscopy and atom probe tomography, Acta Mater. 57 (17) (2009) 5254–5263.
[59] N.V. Thang, X.F. Miao, N.H. van Dijk, E. Bruck, Structural and magnetocaloric properties of (Mn,Fe)2(P,Si) materials with added nitrogen, J. Alloy Compd. 670 (2016) 123–127.
[60] P.D. Nezhadfar, K. Anderson-Wedge, S.R. Daniewicz, N. Phan, S. Shao, N. Shamsaei, Improved high cycle fatigue performance of additively manufactured 17-4 PH stainless steel via in-process refining micro-/defect-structure, Addit. Manuf. 36 (2020) 1–15.
[61] K. Koyama, H. Fujii, Nitrogen gas-solid reaction process and basic magnetism of the interstitially modified rare-earth 3d transition-metal nitrides R2Fe17N3 (R = Y, Ce, Nd, Sm) and Y2Co17N3, Phys. Rev. B 61 (14) (2000) 9475–9493.
[62] T.K. Kim, M. Takahashi, New Magnetic Material Having Ultrahigh Magnetic–Moment, Appl. Phys. Lett. 20 (12) (1972) 492–494.
[63] P.A. Yadav, A.V. Deshmukh, K.P. Adhi, B.B. Kale, N. Basavaih, S.I. Patil, Role of grain size on the magnetic properties of La0.7Sr0.3MnO3, J. Magn. Magn. Mater. 328 (2013) 86–90.
[64] J.A. Turcaud, H.N. Bez, E. Ruiz-Trejo, C.R.H. Bahl, K.K. Nielsen, A. Smith, L.F. Cohen, Influence of manganite powder grain size and Ag-particle coating on the magnetocaloric effect and the active magnetic regenerator performance, Acta Mater. 97 (2015) 413–418.
[65] J. Curiale, M. Granada, H.E. Troiani, R.D. Sanchez, A.G. Leyva, P. Levy, K. Samwer, Magnetic dead layer in ferromagnetic manganite nanoparticles, Appl. Phys. Lett. 95 (4) (2009) 1–3.
[66] K.L. Krycka, R.A. Booth, C.R. Hogg, Y. Ijiri, J.A. Borchers, W.C. Chen, S.M. Watson, M. Laver, T.R. Gentile, L.R. Dedon, S. Harris, J.J. Rhyne, S.A. Majetich, Core-shell magnetic morphology of structurally uniform magnetite nanoparticles, Phys. Rev. Lett. 104 (20) (2010) 1–4.
[67] S. Disch, E. Wetterskog, R.P. Hermann, A. Wiedenmann, U. Vainio, G. Salazar-Alvarez, L. Bergstrom, T. Bruckel, Quantitative spatial magnetization distribution in iron oxide nanocubes and nanospheres by polarized small-angle neutron scattering, New J. Phys. 14 (2012) 1–11.
[68] T. Sarkar, A.K. Raychaudhuri, A.K. Bera, S.M. Yusuf, Effect of size reduction on the ferromagnetism of the manganite La1-xCaxMnO3 (x=0.33), New J. Phys. 12 (2010).

[69] F.M. Li, J.Q. Feng, J. Yi, G. Wang, J.Q. Wang, J.T. Huo, Magnetocaloric properties of LaFe11.4Si1.6 based amorphous alloys, J. Alloy Compd. 845 (2020) 1–7.
[70] J.F. Loffler, J.P. Meier, B. Doudin, J.P. Ansermet, W. Wagner, Random and exchange anisotropy in consolidated nanostructured Fe and Ni: role of grain size and trace oxides on the magnetic properties, Phys. Rev. B 57 (5) (1998) 2915–2924.
[71] S.A. Majetich, J.H. Scott, E.M. Kirkpatrick, K. Chowdary, K. Gallagher, M.E. McHenry, Magnetic nanoparticles and magnetocrystalline anisotropy, Nanostruct. Mater. 9 (1–8) (1997) 291–300.
[72] C. Kittel, Introduction to Solid State Physics, 1976.
[73] H. Yibole, F. Guillou, Y.K. Huang, G.R. Blake, A.J.E. Lefering, N.H. van Dijk, E. Bruck, First-order ferromagnetic transition in single-crystalline (Mn,Fe)2(P,Si), Appl. Phys. Lett. 107 (16) (2015) 1–5.
[74] X.W. Zhou, R.A. Johnson, H.N.G. Wadley, Misfit-energy-increasing dislocations in vapor-deposited CoFe/NiFe multilayers, Phys. Rev. B 69 (14) (2004) 1–10.
[75] M.E. Gruner, W. Keune, B. Roldan Cuenya, C. Weis, J. Landers, S.I. Makarov, D. Klar, M.Y. Hu, E.E. Alp, J. Zhao, M. Krautz, O. Gutfleisch, H. Wende, Element-resolved thermodynamics of magnetocaloric LaFe13-xSix, Phys. Rev. Lett. 114 (5) (2015) 1–6.
[76] Y.H. Qu, D.Y. Cong, X.M. Sun, Z.H. Nie, W.Y. Gui, R.G. Li, Y. Ren, Y.D. Wang, Giant and reversible room-temperature magnetocaloric effect in Ti-doped Ni–Co-Mn-Sn magnetic shape memory alloys, Acta Mater. 134 (2017) 236–248.
[77] A. Zelenakova, P. Hrubovcak, O. Kapusta, V. Zelenak, V. Franco, Large magnetocaloric effect in fine Gd2O3 nanoparticles embedded in porous silica matrix, Appl. Phys. Lett. 109 (12) (2016) 122412.
[78] J. Li, S. Ma, H. Wang, W.J. Gong, J.J. Jiang, S.J. Li, Y. Wang, D.Y. Geng, Z.D. Zhang, Enhanced cryogenic magnetocaloric effect induced by small size GdNi5 nanoparticles, J. Mater. Sci. Technol. 30 (10) (2014) 973–978.
[79] D. Doblas, L.M. Moreno-Ramirez, V. Franco, A. Conde, A.V. Svalov, G.V. Kurlyandskaya, Nanostructuring as a procedure to control the field dependence of the magnetocaloric effect, Mater. Des. 114 (2017) 214–219.
[80] A.F. Manchon-Gordon, A. Gomez, J.J. Ipus, J.S. Blazquez, C.F. Conde, A. Conde, Milling effects on the distribution of Curie temperatures and magnetic properties of Ni-doped La0.7Ca0.3MnO3 compounds, J. Alloy Compd. 848 (2020) 1–7.
[81] D.M. Rajkumar, M.M. Raja, R. Gopalan, V. Chandrasekaran, Magnetocaloric effect in high-energy ball-milled Gd5Si2Ge2 and Gd5Si2Ge2/Fe nanopowders, J. Magn. Magn. Mater. 320 (8) (2008) 1479–1484.
[82] H. Yang, Y.H. Zhu, T. Xian, J.L. Jiang, Synthesis and magnetocaloric properties of La0.7Ca0.3MnO3 nanoparticles with different sizes, J. Alloy Compd. 555 (2013) 150–155.
[83] S.P. Mathew, S.N. Kaul, Tuning magnetocaloric effect with nanocrystallite size, Appl. Phys. Lett. 98 (17) (2011) 1–3.
[84] J.M. Logan, D. Rosenmann, T. Sangpo, M.V. Holt, P. Fuesz, I. McNulty, Tungsten-encapsulated gadolinium nanoislands with enhanced magnetocaloric response, Appl. Phys. Lett. 111 (1) (2017) 1–5.
[85] J.Y. Cheng, T. Li, S. Ullah, F. Luo, H. Wang, M. Yan, G.P. Zheng, Giant magnetocaloric effect in nanostructured Fe-Co-P amorphous alloys enabled through pulse electrodeposition, Nanotechnology 31 (38) (2020) 1–9.
[86] V. Chaudhary, R.V. Ramanujan, Magnetic and structural properties of high relative cooling power (Fe70Ni30)92Mn8 magnetocaloric nanoparticles, J. Phys. D 48 (30) (2015) 1–7.
[87] V. Chaudhary, R.V. Ramanujan, Magnetocaloric properties of Fe-Ni-Cr nanoparticles for active cooling, Sci. Rep. 6 (2016) 1–9.
[88] P. Alvarez-Alonso, J.L.S. Llamazares, C.F. Sanchez-Valdes, G.J. Cuello, V. Franco, P. Gorria, J.A. Blanco, On the broadening of the magnetic entropy change due to Curie temperature distribution, J. Appl. Phys. 115 (17) (2014) 1–3.
[89] J. Ipus, H. Ucar, M. McHenry, Near room temperature magnetocaloric response of an (FeNi)ZrB alloy, IEEE Trans. Magn. 47 (10) (2011) 2494–2497.
[90] J.Y. Law, V. Franco, L.M. Moreno-Ramirez, A. Conde, D.Y. Karpenkov, I. Radulov, K.P. Skokov, O. Gutfleisch, A quantitative criterion for determining the order of magnetic phase transitions using the magnetocaloric effect, Nat. Commun. 9 (2018) 1–9.
[91] V. Franco, J.S. Blazquez, A. Conde, Field dependence of the magnetocaloric effect in materials with a second order phase transition: a master curve for the magnetic entropy change, Appl. Phys. Lett. 89 (22) (2006) 1–3.
[92] V. Franco, A. Conde, Scaling laws for the magnetocaloric effect in second order phase transitions: from physics to applications for the characterization of materials, Int. J. Refrig. 33 (3) (2010) 465–473.
[93] J.A. Nelson, L.H. Bennett, M.J. Wagner, Solution synthesis of gadolinium nanoparticles, J. Am. Chem. Soc. 124 (12) (2002) 2979–2983.
[94] A.H. Lu, E.L. Salabas, F. Schuth, Magnetic nanoparticles: synthesis, protection, functionalization, and application, Angew. Chem. Int. Edit. 46 (8) (2007) 1222–1244.
[95] V. Sepelak, A. Feldhoff, P. Heitjans, F. Krumeich, D. Menzel, F.J. Litterst, I. Bergmann, K.D. Becker, Nonequilibrium cation distribution, canted spin arrangement, and enhanced magnetization in nanosized MgFe2O4 prepared by a one-step mechanochemical route, Chem. Mater. 18 (13) (2006) 3057–3067.
[96] A.G. Roca, J.F. Marco, M.D. Morales, C.J. Serna, Effect of nature and particle size on properties of uniform magnetite and maghemite nanoparticles, J. Phys. Chem. C 111 (50) (2007) 18577–18584.
[97] P.C. Morais, A.L. Tronconi, K.S. Neto, Temperature-dependence of the mossbauer linewidth of superparamagnetic particles of ferric hydroxysulfate, J. Appl. Phys. 57 (4) (1985) 1291–1293.
[98] M.J.N. Isfahani, M. Myndyk, V. Sepelak, J. Amighian, A Mossbauer effect investigation of the formation of MnZn nanoferrite phase, J. Alloy Compd. 470 (1–2) (2009) 434–437.
[99] P Roggwill, W. Kundig, Mossbauer-spectra of superparamagnetic Fe3O4, Solid State Commun. 12 (9) (1973) 901–903.
[100] J.T. Batley, M. Nguyen, I. Kamboj, C. Korostynski, E.S. Aydil, C. Leighton, Quantitative understanding of superparamagnetic blocking in thoroughly characterized Ni nanoparticle assemblies, Chem. Mater. 32 (15) (2020) 6494–6506.
[101] M. Tadic, S. Kralj, M. Jagodic, D. Hanzel, D. Makovec, Magnetic properties of novel superparamagnetic iron oxide nanoclusters and their peculiarity under annealing treatment, Appl. Surf. Sci. 322 (2014) 255–264.